



Towards Real-World Ultrasound Understanding: Large Vision-Language Models from Multi-Image Examinations with Long-Form Reports

Bingcong Yan¹, Chunlei Li¹, Jingliang Hu¹, Yilei Shi¹, Xiao Xiang Zhu², Lichao Mou^{1,*}

¹MedAI Technology (Wuxi) Co. Ltd.

²Technical University of Munich

*Correspondence: lichao.mou@gmail.com

<https://medai-t.github.io/LUMI/>

Abstract

Large vision-language models (LVLMs) have achieved strong performance across many medical imaging tasks, yet their application to ultrasound remains limited due to its inherent complexity and variability. In this work, we revisit what is truly needed to enable real-world ultrasound understanding. Instead of introducing complex architectures or elaborate training strategies, we show that data scale and clinically faithful data alignment are the key factors. We construct a large-scale dataset of 1.5M real-world ultrasound examinations, containing 17.7M images, multi-organ coverage, and paired uncurated clinical reports. Crucially, we organize the data at the examination level, aligning multiple images with their corresponding reports to reflect real clinical workflows. We then fine-tune a standard LVLM using low-rank adaptation (LoRA) on this dataset without task-specific modifications. Surprisingly, this simple recipe already leads to strong performance across diverse ultrasound understanding tasks, outperforming prior methods designed with more complex pipelines. Beyond these results, we present model and data scaling analyses that provide insights into the role of scale in ultrasound LVLMs.

1 Introduction

Large vision-language models (LVLMs) have recently demonstrated remarkable performance across both general-domain [1, 2, 3, 4] and medical imaging tasks [5, 6, 7, 8, 9, 10, 11, 12], including computed tomography (CT), magnetic resonance imaging (MRI), X-ray, and positron emission tomography (PET). By jointly modeling visual content and textual descriptions, these models enable a wide range of applications such as visual question answering, report generation, and clinical decision support.

Despite this progress, extending LVLMs to ultrasound remains highly challenging. Unlike CT, MRI, and X-ray, which provide relatively standardized and global anatomical views, ultrasound has a limited field of view and is inherently examination-centric. In routine clinical practice, a single ultrasound examination typically consists of multiple images acquired from different viewpoints, often covering multiple organs. Even for a single organ, several views are usually required for comprehensive assessment. Furthermore, ultrasound imaging is highly operator-dependent and frequently affected by noise, artifacts, acoustic shadowing, and varying acquisition protocols, leading to substantially greater complexity and variability compared with other imaging modalities.

Several recent studies have begun exploring LVLMs for ultrasound understanding¹. For example, [20] fine-tunes Qwen2.5-VL using ultrasound textbooks and image-text pairs, primarily based on single-image captioning data. Similarly, [21] trains a multimodal large language model (MLLM) for ultrasound image captioning and question answering. [22] investigates chain-of-thought (CoT) fine-tuning of Qwen2.5-VL-7B-Instruct for ultrasound reasoning at the image level. [23] extends a base

¹We note that recent work has also explored other types of foundation models for ultrasound imaging, including vision foundation models [13, 14] and CLIP-style models [15, 16, 17, 18, 19]. While complementary to LVLMs, these approaches fall outside the scope of this work and are not discussed in detail here.

LVLMM to support not only captioning but also segmentation and detection, albeit still within single-image settings. [24] further incorporates organ-level image-text pairs with multiple images per sample to train a customized Qwen2-VL model. While these efforts demonstrate promising early results, they are still developed under relatively simplified settings, focusing on either single images or single organs. In real-world clinical workflows, ultrasound examinations naturally involve complex relationships among multiple images, multiple organs, and long-form reports. For instance, abdominal ultrasound examinations routinely include the liver, gallbladder, pancreas, spleen, and kidneys, with different organs often co-occurring within the same image.

The discrepancy between existing training settings and practical clinical scenarios remains largely underexplored. More fundamentally, an open question is whether advancing ultrasound LVLMMs truly requires sophisticated model architectures or whether data scale and clinically grounded data alignment play a more decisive role.

In this work, we take a step toward real-world ultrasound understanding by training an LVLMM on large-scale ultrasound data collected in the wild. Our framework leverages clinically faithful examination-level supervision, where multiple images from the same examination are paired with their corresponding clinical report. By modeling the relationships between these images and the associated report, the model learns to perform more realistic and comprehensive ultrasound reasoning.

Our contributions are summarized as follows:

- We move beyond image-level or organ-level supervision and study LVLMMs under realistic clinical scenarios involving multi-image examinations and rich long-form textual supervision.
- We construct a large-scale ultrasound dataset containing nearly 1.5 million examinations, 17.7 million images, over 14 organs, and extensive clinical reports collected from real-world practice.
- We train an LVLMM on this dataset, which we call LUMI, and benchmark a broad range of large models, achieving state-of-the-art performance.

2 Dataset

2.1 Data Collection

2.1.1 Sources and Composition

Our dataset consists of de-identified ultrasound examinations collected from multiple large medical institutions between 2014 and 2025. The data is organized at the examination level, where each case contains the complete set of ultrasound images together with the corresponding detailed clinical report.

The dataset covers five major clinical domains, including thyroid, breast, upper abdomen, gynecology, and male urinary examinations. The examinations involve a diverse set of anatomical structures, including the liver, gallbladder, spleen, pancreas, thyroid, cervical lymph nodes, axillary lymph nodes, breast, kidneys, uterus, ovaries, bladder, prostate, and carotid arteries, among others. A key characteristic of real-world ultrasound imaging is the frequent co-occurrence of multiple organs within the same scanning plane, which is naturally preserved in our dataset. For example, the liver and gallbladder commonly appear together in upper abdominal scans, while the uterus and ovaries are often jointly visualized in gynecological examinations.

2.1.2 Curation and Preprocessing

To ensure data quality, consistency, and privacy compliance, we applied a multi-stage curation and preprocessing pipeline:

- **Privacy and anonymization.** All personally identifiable information (PII) was rigorously removed from both imaging data and textual reports, including patient names, identification numbers, and contact information.
- **Case filtering.** We excluded cases with missing images or reports. Cases containing an anomalously large number of images (> 32) were removed. We further discarded reports that were excessively short (length < 5 characters), which typically provide insufficient clinical information, as well as excessively long reports (length > 3000 characters), which often contain redundant or non-standard content.

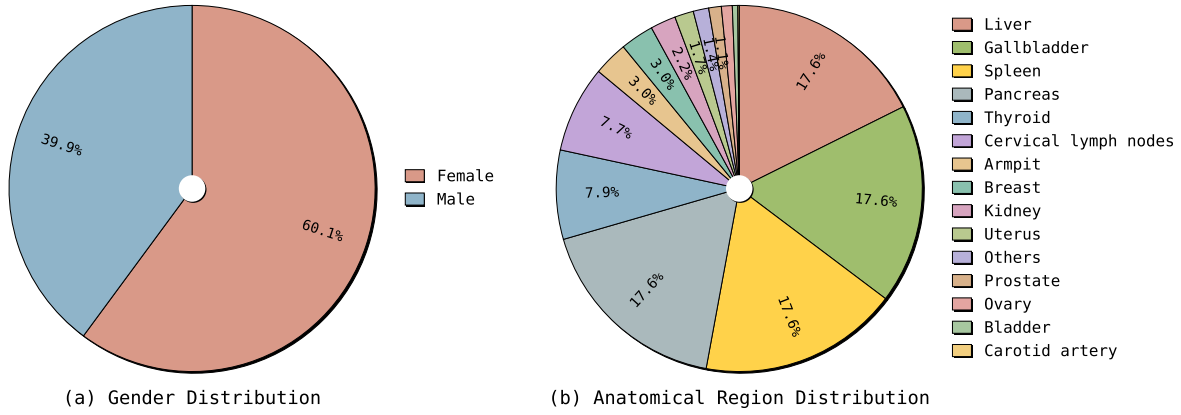


Figure 1: Demographic and anatomical distributions of the ultrasound dataset. (a) Patient gender distribution. (b) Distribution of anatomical structures covered by the examinations.

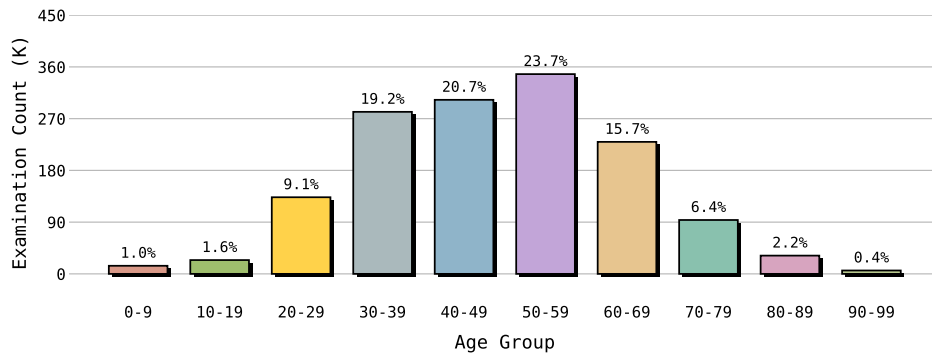


Figure 2: Age distribution of patients in the dataset.

- **Standardization.** All ultrasound images were converted into a unified format and resolution to ensure consistency across institutions and acquisition devices. Textual reports were further cleaned by removing institutional metadata, such as hospital and department identifiers, followed by formatting normalization and tokenization.

2.2 Dataset Statistics

2.2.1 Scale and Basic Demographics

The final curated dataset contains 1,464,461 examination cases and 17,673,019 ultrasound images, with an average of 12.1 images per examination. The gender distribution of the patient cohort is illustrated in Figure 1, while the age distribution is shown in Figure 2.

2.2.2 Examination Distribution

The distribution of examination categories is presented in Figure 1. Upper abdomen examinations constitute the largest portion of the dataset, followed by thyroid examinations. Breast, gynecology, and male urinary examinations are also well represented, providing broad clinical coverage for model training and evaluation.

2.2.3 Text Report Characteristics

The associated clinical reports exhibit substantial variability in descriptive detail and writing style, with an average length of 198 characters (in Chinese). This diversity reflects the nuanced and personalized nature of real-world clinical reporting.

2.2.4 Dataset Splits

We constructed the test set using stratified sampling based on the primary examination category to ensure balanced evaluation across all major clinical domains. The detailed composition of the test set is summarized in Table 1. The remaining data was randomly divided into training and validation sets.

Table 1: Composition of the test set by examination category.

Examination Type	Number of Cases
Upper Abdomen	331
Thyroid	200
Breast	182
Gynecology	200
Male Urinary	62

3 Model Training

We adopt Qwen3-VL-4B-Instruct as the base LVLm and adapt it to ultrasound examination understanding through supervised fine-tuning. Given a multi-image ultrasound examination, the model takes ultrasound images together with a textual instruction as input and is trained to autoregressively generate the corresponding clinical report or target response.

To improve training efficiency while preserving the general multimodal capabilities of the pretrained model, we employ low-rank adaptation (LoRA) for parameter-efficient fine-tuning. Specifically, LoRA adapters are inserted into the self-attention projection layers of the decoder, including `q_proj`, `k_proj`, `v_proj`, and `o_proj`, while all remaining pretrained parameters are frozen. The LoRA rank is set to $r = 16$, with a scaling factor $\alpha = 32$ and a dropout rate of 0.1. The model is optimized using the standard autoregressive cross-entropy loss over the target token sequence.

Training is conducted for 182,936 iterations on NVIDIA GPUs using `bfloat16` mixed-precision computation. We optimize the model using AdamW with a learning rate of 1×10^{-4} , a weight decay of 0.01, and a cosine learning-rate schedule with a warm-up ratio of 0.03. The batch size is set to 8 without additional gradient accumulation. To improve training stability, gradient clipping with a maximum norm of 1.0 is applied. The maximum sequence length is set to 4,096 tokens. For visual inputs, we constrain image resolution by limiting the minimum and maximum numbers of pixels to 784 and 112,896, respectively.

4 Experiments

4.1 Baselines

We compare LUMI against a diverse set of state-of-the-art LVLms, including both general-purpose and medical-domain models. The baselines include the InternVL3.5 series (1B–38B) [1], the Qwen3.5 series (0.8B–35B) [2], Kimi-VL [3], HuatuoGPT-Vision (7B and 34B) [5], Lingshu (7B and 32B) [6], MedGemma [7], and EchoVLM [24], a publicly available ultrasound-specific vision-language model. We additionally considered several other representative LVLms, including the LLaVA-1.6-Vicuna series (7B and 13B) [25], the Janus-Pro series (1B and 7B) [26], LLaVA-Med v1.5 [9], HealthGPT [12], and Med-Flamingo [10]. These models were excluded from the final comparison because they either do not support the long input sequences required by multi-image ultrasound examinations or produce unstable outputs (e.g., garbled text) when processing a large number of images.

4.2 Main Results

We conduct a comprehensive evaluation across five examination categories: Thyroid, Breast, Upper Abdomen, Gynecology, and Male Urinary. Following prior report generation studies, we adopt BLEU-1/2/3/4, ROUGE-L, METEOR, and BERTScore as evaluation metrics.

To further assess clinical correctness, we introduce the F1 score. Specifically, both the generated report and the corresponding ground-truth report are provided to an LLM-based evaluator, which

Table 2: Performance comparison of general-purpose (♠), medical-domain-specific (♣) LVLMs across different examination types. BL, RG-L, MTR, BS, and F1 denote BLEU, ROUGE-L, METEOR, BERTScore, and F1 score, respectively. **Note.** Representative LVLMs, including LLaVA-1.6-Vicuna, Janus-Pro, LLaVA-Med v1.5, HealthGPT, and Med-Flamingo, were excluded due to insufficient long-context support for multi-image ultrasound examinations or unstable outputs when processing a large number of images.

	Thyroid					Breast					Upper Abdomen													
	BL-1	BL-2	BL-3	BL-4	RG-L	MTR	BS	F1	BL-1	BL-2	BL-3	BL-4	RG-L	MTR	BS	F1	BL-1	BL-2	BL-3	BL-4	RG-L	MTR	BS	F1
InternVL3.5-1B-Instruct	0.257	0.160	0.107	0.075	0.252	0.219	0.724	0.287	0.179	0.122	0.083	0.053	0.294	0.249	0.716	0.040	0.109	0.060	0.037	0.020	0.278	0.171	0.695	0.064
InternVL3.5-2B-Instruct	0.227	0.140	0.092	0.061	0.250	0.221	0.717	0.306	0.295	0.180	0.120	0.075	0.272	0.242	0.715	0.152	0.309	0.206	0.142	0.097	0.300	0.235	0.745	0.065
InternVL3.5-4B-Instruct	0.210	0.134	0.088	0.060	0.260	0.219	0.724	0.298	0.262	0.150	0.110	0.069	0.271	0.251	0.719	0.140	0.326	0.211	0.145	0.100	0.292	0.269	0.742	0.132
InternVL3.5-8B-Instruct	0.323	0.207	0.136	0.089	0.261	0.240	0.744	0.334	0.345	0.234	0.164	0.107	0.319	0.279	0.744	0.127	0.377	0.255	0.182	0.131	0.320	0.286	0.763	0.054
InternVL3.5-14B-Instruct	0.295	0.187	0.126	0.086	0.245	0.215	0.719	0.298	0.316	0.201	0.136	0.087	0.295	0.270	0.734	0.372	0.375	0.235	0.155	0.101	0.295	0.269	0.747	0.112
InternVL3.5-30B-A3B-Instruct	0.331	0.210	0.139	0.095	0.256	0.237	0.728	0.285	0.352	0.228	0.153	0.096	0.340	0.274	0.747	0.380	0.351	0.243	0.174	0.125	0.343	0.291	0.764	0.079
InternVL3.5-38B-Instruct	0.311	0.189	0.125	0.084	0.239	0.213	0.709	0.278	0.317	0.213	0.148	0.097	0.322	0.286	0.735	0.324	0.329	0.206	0.139	0.092	0.273	0.252	0.724	0.074
Qwen3.5-0.8B	0.247	0.134	0.085	0.054	0.199	0.166	0.695	0.202	0.188	0.108	0.068	0.040	0.223	0.194	0.695	0.124	0.162	0.084	0.051	0.029	0.183	0.168	0.683	0.327
Qwen3.5-2B	0.238	0.134	0.085	0.055	0.205	0.205	0.701	0.219	0.203	0.120	0.077	0.047	0.224	0.236	0.698	0.084	0.205	0.109	0.065	0.038	0.214	0.229	0.702	0.051
Qwen3.5-4B	0.229	0.125	0.075	0.044	0.203	0.220	0.706	0.178	0.181	0.110	0.071	0.043	0.248	0.265	0.710	0.467	0.210	0.115	0.066	0.037	0.231	0.257	0.714	0.228
Qwen3.5-9B	0.307	0.181	0.116	0.075	0.234	0.232	0.720	0.323	0.247	0.154	0.101	0.065	0.280	0.293	0.732	0.232	0.251	0.145	0.090	0.055	0.280	0.290	0.733	0.182
Qwen3.5-27B	0.362	0.226	0.146	0.094	0.268	0.254	0.737	0.335	0.325	0.220	0.153	0.105	0.352	0.353	0.762	0.283	0.386	0.257	0.176	0.119	0.372	0.363	0.777	0.293
Qwen3.5-35B-A3B	0.284	0.172	0.106	0.066	0.243	0.260	0.726	0.338	0.237	0.149	0.098	0.061	0.288	0.312	0.731	0.332	0.295	0.184	0.117	0.074	0.303	0.321	0.751	0.183
Kimi-VL-A3B-Instruct-16B	0.057	0.035	0.023	0.016	0.264	0.189	0.716	0.235	0.133	0.094	0.066	0.044	0.322	0.261	0.736	0.273	0.401	0.282	0.201	0.146	0.363	0.303	0.776	0.163
HuatuoGPT-Vision-7B	0.084	0.054	0.039	0.027	0.237	0.142	0.703	0.457	0.239	0.153	0.106	0.067	0.260	0.221	0.717	0.137	0.147	0.098	0.070	0.049	0.275	0.205	0.737	0.109
HuatuoGPT-Vision-34B	0.253	0.164	0.113	0.081	0.266	0.223	0.736	0.317	0.323	0.206	0.140	0.087	0.297	0.263	0.728	0.148	0.302	0.201	0.142	0.099	0.300	0.256	0.754	0.075
Lingshu-7B	0.252	0.155	0.105	0.070	0.239	0.184	0.708	0.339	0.297	0.193	0.136	0.090	0.286	0.249	0.728	0.281	0.377	0.243	0.163	0.107	0.271	0.275	0.748	0.067
Lingshu-32B	0.294	0.183	0.119	0.078	0.268	0.229	0.733	0.223	0.318	0.204	0.137	0.086	0.316	0.271	0.744	0.300	0.340	0.219	0.141	0.094	0.290	0.277	0.740	0.178
medgemma-4b-it	0.131	0.059	0.032	0.014	0.135	0.143	0.632	0.149	0.107	0.055	0.032	0.016	0.151	0.148	0.627	0.227	0.113	0.055	0.031	0.017	0.173	0.164	0.645	0.068
EchoVLM	0.223	0.129	0.078	0.043	0.293	0.218	0.731	0.286	0.112	0.072	0.050	0.034	0.366	0.216	0.745	0.427	0.183	0.116	0.077	0.054	0.358	0.227	0.745	0.061
LUMI	0.796	0.738	0.682	0.630	0.757	0.780	0.935	0.667	0.724	0.653	0.592	0.538	0.758	0.721	0.916	0.727	0.715	0.665	0.623	0.587	0.784	0.713	0.907	0.714
	Gynecology					Male Urinary					AVG													
	BL-1	BL-2	BL-3	BL-4	RG-L	MTR	BS	F1	BL-1	BL-2	BL-3	BL-4	RG-L	MTR	BS	F1	BL-1	BL-2	BL-3	BL-4	RG-L	MTR	BS	F1
InternVL3.5-1B-Instruct	0.063	0.029	0.017	0.009	0.270	0.124	0.667	0.184	0.087	0.039	0.020	0.008	0.222	0.109	0.654	0.040	0.139	0.082	0.053	0.033	0.263	0.174	0.691	0.123
InternVL3.5-2B-Instruct	0.137	0.085	0.058	0.039	0.273	0.211	0.712	0.173	0.212	0.124	0.086	0.062	0.224	0.152	0.693	0.023	0.236	0.147	0.100	0.067	0.264	0.212	0.717	0.144
InternVL3.5-4B-Instruct	0.265	0.155	0.100	0.060	0.267	0.229	0.720	0.230	0.229	0.139	0.097	0.069	0.231	0.169	0.696	0.047	0.258	0.161	0.108	0.072	0.264	0.227	0.719	0.169
InternVL3.5-8B-Instruct	0.292	0.191	0.129	0.087	0.312	0.265	0.740	0.308	0.157	0.096	0.067	0.047	0.227	0.163	0.705	0.039	0.299	0.197	0.136	0.092	0.288	0.247	0.739	0.172
InternVL3.5-14B-Instruct	0.318	0.196	0.126	0.082	0.302	0.269	0.741	0.187	0.231	0.140	0.094	0.064	0.265	0.184	0.708	0.011	0.307	0.192	0.127	0.084	0.280	0.243	0.730	0.182
InternVL3.5-30B-A3B-Instruct	0.331	0.205	0.132	0.085	0.327	0.266	0.760	0.232	0.209	0.131	0.088	0.058	0.285	0.186	0.725	0.058	0.315	0.203	0.137	0.092	0.310	0.251	0.745	0.207
InternVL3.5-38B-Instruct	0.370	0.239	0.157	0.104	0.350	0.296	0.766	0.254	0.237	0.148	0.098	0.061	0.304	0.199	0.722	0.011	0.313	0.199	0.133	0.088	0.298	0.249	0.731	0.191
Qwen3.5-0.8B	0.167	0.093	0.058	0.032	0.210	0.183	0.681	0.359	0.213	0.106	0.063	0.034	0.186	0.132	0.669	0.012	0.195	0.105	0.065	0.038	0.200	0.169	0.684	0.205
Qwen3.5-2B	0.165	0.090	0.055	0.031	0.213	0.211	0.680	0.121	0.248	0.130	0.077	0.043	0.217	0.184	0.686	0.022	0.212	0.117	0.072	0.043	0.215	0.213	0.693	0.099
Qwen3.5-4B	0.149	0.081	0.048	0.027	0.249	0.243	0.706	0.384	0.304	0.162	0.093	0.051	0.238	0.198	0.701	0.044	0.214	0.119	0.070	0.040	0.234	0.237	0.707	0.260
Qwen3.5-9B	0.224	0.127	0.076	0.046	0.273	0.270	0.720	0.201	0.288	0.156	0.096	0.062	0.261	0.217	0.710	0.172	0.263	0.153	0.096	0.061	0.265	0.261	0.723	0.222
Qwen3.5-27B	0.274	0.163	0.099	0.061	0.331	0.306	0.746	0.224	0.378	0.230	0.152	0.102	0.355	0.275	0.747	0.402	0.345	0.220	0.145	0.096	0.335	0.310	0.754	0.307
Qwen3.5-35B-A3B	0.241	0.143	0.088	0.054	0.287	0.284	0.730	0.207	0.318	0.182	0.111	0.069	0.312	0.267	0.733	0.370	0.275	0.166	0.104	0.065	0.287	0.289	0.734	0.286
Kimi-VL-A3B-Instruct-16B	0.313	0.211	0.148	0.104	0.333	0.265	0.749	0.322	0.213	0.132	0.088	0.056	0.264	0.211	0.711	0.069	0.223	0.151	0.105	0.073	0.309	0.238	0.738	0.212
HuatuoGPT-Vision-7B	0.258	0.164	0.114	0.080	0.301	0.243	0.728	0.200	0.120	0.072	0.045	0.027	0.240	0.143	0.699	0.127	0.170	0.108	0.075	0.050	0.263	0.191	0.717	0.206
HuatuoGPT-Vision-34B	0.273	0.167	0.110	0.070	0.277	0.238	0.729	0.196	0.177	0.109	0.072	0.046	0.283	0.177	0.711	0.109	0.266	0.169	0.115	0.076	0.285	0.232	0.732	0.169
Lingshu-7B	0.290	0.184	0.124	0.084	0.288	0.265	0.742	0.201	0.162	0.092	0.058	0.036	0.219	0.143	0.691	0.120	0.276	0.173	0.117	0.078	0.260	0.223	0.723	0.202
Lingshu-32B	0.341	0.219	0.149	0.104	0.309	0.272	0.753	0.146	0.209	0.116	0.074	0.046	0.211	0.145	0.679	0.122	0.300	0.188	0.124	0.081	0.279	0.239	0.730	0.194
medgemma-4b-it	0.129	0.059	0.033	0.014	0.169	0.159	0.636	0.181	0.154	0.066	0.035	0.015	0.143	0.127	0.622	0.000	0.127	0.059	0.033	0.015	0.153	0.150	0.632	0.125
EchoVLM	0.143	0.081	0.049	0.030	0.333	0.206	0.729	0.335	0.197	0.114	0.072	0.043	0.268	0.163	0.704	0.058	0.172	0.102	0.065	0.041	0.323	0.206	0.731	0.233
LUMI	0.643	0.579	0.527	0.482	0.734	0.637	0.894	0.565	0.875	0.858	0.840	0.821	0.912	0.874	0.948	0.850	0.751	0.699	0.653	0.612	0.789	0.745	0.920	0.705

evaluates the consistency of lesion identification and diagnostic conclusions between the two reports. Precision, recall, and F1 scores are then computed on a per-lesion basis, providing a more direct measure of clinical reliability than conventional text-similarity metrics.

The quantitative results are summarized in Table 2. LUMI achieves state-of-the-art performance across all five examination categories and consistently outperforms the competing models on both natural language generation and clinical metrics. Notably, LUMI ranks first across all evaluation metrics in the average (AVG.) column. The improvements are particularly pronounced on higher-order natural language generation metrics and the F1 score, indicating that LUMI not only produces linguistically accurate reports but also captures clinically relevant findings with greater fidelity.

4.3 Qualitative Analysis

We provide representative case studies in the Appendix to compare the report generation capabilities of LUMI with those of leading baseline models. The examples illustrate that LUMI generates reports that are more complete, clinically coherent, and better aligned with the underlying ultrasound findings.

4.4 Discussion

4.4.1 Comparison with Medical-Domain Models

LUMI consistently outperforms medical-domain LVLMs, including HuatuoGPT-Vision, Lingshu, and EchoVLM. These results suggest that large-scale ultrasound-specific supervision plays a crucial role in developing clinically effective ultrasound understanding models, beyond the benefits provided by general medical pretraining alone.

4.4.2 Clinical Fidelity

While several baseline models are capable of generating fluent and well-structured reports, they frequently omit clinically important findings or introduce unsupported diagnostic statements. In contrast, LUMI demonstrates stronger factual consistency with the reference reports and better adherence to clinical reporting conventions, leading to improved diagnostic reliability.

4.4.3 Model Scaling

We further investigate the impact of model scale. Under the same experimental setting and training recipe, we train 2B and 8B variants and compare them with the 4B model. As shown in Figure 3, the 2B model consistently underperforms the 4B model across all evaluation metrics, indicating that increasing model capacity benefits ultrasound understanding. The improvement is particularly pronounced in terms of the F1 score: the 2B model achieves an F1 score of 0.614, whereas the 4B model reaches 0.705, corresponding to an absolute gain of 0.091. However, scaling the model further from 4B to 8B yields no substantial performance improvement across the evaluation metrics. This suggests that performance gains saturate beyond the 4B scale under our current training setup and dataset.

4.4.4 Data Scaling

We also analyze the effect of data scale by training models using 25%, 50%, 75%, and 100% of the training data. As shown in Figure 3, performance consistently improves as the amount of training data increases, highlighting the importance of large-scale, domain-specific data for ultrasound LVLMs. Interestingly, even with a relatively small training set, the model already achieves competitive scores on natural language generation metrics such as BERTScore. In contrast, the clinical F1 score remains substantially lower, suggesting that the generated reports may be linguistically and structurally plausible while still lacking sufficient diagnostic accuracy. Notably, at the largest training scale evaluated (approximately 1.5 million samples), the performance curves for most evaluation metrics—particularly the clinical F1 score—show no clear sign of saturation. This finding suggests that further scaling the training data could yield additional performance gains.

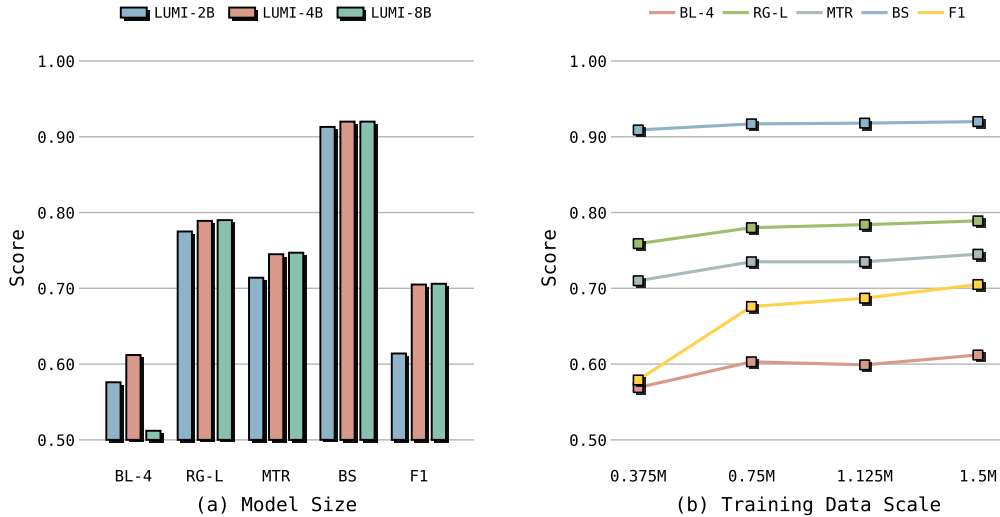


Figure 3: Performance under different model and data scales. (a) Model size. (b) Training data scale. BL, RG-L, MTR, BS, and F1 denote BLEU, ROUGE-L, METEOR, BERTScore, and F1 score, respectively.

4.4.5 Limitation

Since LUMI is trained on paired data consisting of all images from a complete ultrasound examination and the corresponding report, it may hallucinate findings when presented with severely incomplete image sets at inference time.

5 Conclusion

In this work, we present LUMI, an LVLm specialized for real-world ultrasound understanding. To support this effort, we construct a large-scale ultrasound dataset consisting of nearly 1.5 million examinations and 17.7 million images spanning multiple anatomical regions, with examination-level image-text alignment that reflects real clinical workflows. Experimental results demonstrate that LUMI achieves state-of-the-art performance across a wide range of natural language generation and clinical metrics, outperforming both general-purpose and medical-domain LVLms. Furthermore, our model and data scaling analyses provide insights into the role of scale in advancing LVLms for ultrasound and other medical imaging applications.

References

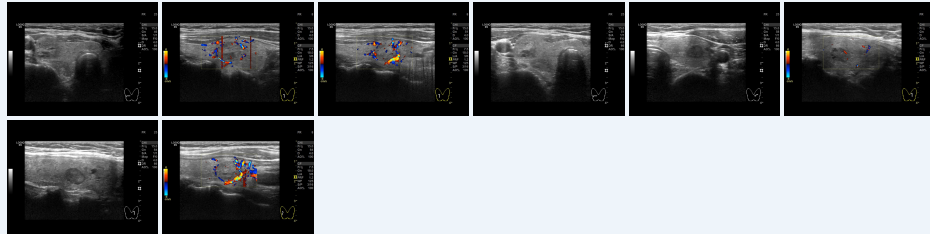
- [1] Weiyun Wang, Zhangwei Gao, Lixin Gu, Hengjun Pu, Long Cui, Xingguang Wei, Zhaoyang Liu, Linglin Jing, Shenglong Ye, Jie Shao, Zhaokai Wang, Zhe Chen, Hongjie Zhang, Ganlin Yang, Haomin Wang, Qi Wei, Jinhui Yin, Wenhao Li, Erfei Cui, Guanzhou Chen, Zichen Ding, Changyao Tian, Zhenyu Wu, JingJing Xie, Zehao Li, Bowen Yang, Yuchen Duan, Xuehui Wang, Zhi Hou, Haoran Hao, Tianyi Zhang, Songze Li, Xiangyu Zhao, Haodong Duan, Nianchen Deng, Bin Fu, Yanan He, Yi Wang, Conghui He, Botian Shi, Junjun He, Yingtong Xiong, Han Lv, Lijun Wu, Wenqi Shao, Kaipeng Zhang, Huipeng Deng, Biqing Qi, Jiaye Ge, Qipeng Guo, Wenwei Zhang, Songyang Zhang, Maosong Cao, Junyao Lin, Kexian Tang, Jianfei Gao, Haiyan Huang, Yuzhe Gu, Chengqi Lyu, Huanze Tang, Rui Wang, Haijun Lv, Wanli Ouyang, Limin Wang, Min Dou, Xizhou Zhu, Tong Lu, Dahua Lin, Jifeng Dai, Weijie Su, Bowen Zhou, Kai Chen, Yu Qiao, Wenhai Wang, and Gen Luo. InternVL3.5: Advancing open-source multimodal models in versatility, reasoning, and efficiency. *arXiv preprint arXiv:2508.18265*, 2025.
- [2] Qwen Team. Qwen3-VL technical report. *arXiv preprint arXiv:2511.21631*, 2025.

- [3] Kimi Team. Kimi-VL technical report. *arXiv preprint arXiv:2504.07491*, 2025.
- [4] Bo Li, Yuanhan Zhang, Dong Guo, Renrui Zhang, Feng Li, Hao Zhang, Kaichen Zhang, Peiyuan Zhang, Yanwei Li, Ziwei Liu, and Chunyuan Li. LLaVA-OneVision: Easy visual task transfer. *Transactions on Machine Learning Research*, 2025.
- [5] Junying Chen, Ruyi Ouyang, Anningzhe Gao, Shunian Chen, Guiming Hardy Chen, Xidong Wang, Ruifei Zhang, Zhenyang Cai, Ke Ji, Guangjun Yu, Xiang Wan, and Benyou Wang. HuatuoGPT-Vision: Towards injecting medical visual knowledge into multimodal LLMs at scale. *arXiv preprint arXiv:2406.19280*, 2024.
- [6] LLaVA Team, Weiwen Xu, Hou Pong Chan, Long Li, Mahani Aljunied, Ruifeng Yuan, Jianyu Wang, Chenghao Xiao, Guizhen Chen, Chaoqun Liu, Zhaodonghui Li, Yu Sun, Junao Shen, Chaojun Wang, Jie Tan, Deli Zhao, Tingyang Xu, Hao Zhang, and Yu Rong. Lingshu: A generalist foundation model for unified multimodal medical understanding and reasoning. *arXiv preprint arXiv:2506.07044*, 2025.
- [7] Andrew Sellergren, Chufan Gao, Fereshteh Mahvar, Timo Kohlberger, Fayaz Jamil, Madeleine Traverse, Alberto Tono, Bashir Sadjad, Lin Yang, Charles Lau, Liron Yatziv, Tiffany L. Chen, Bram Sterling, Kenneth Philbrick, Richa Tiwari, Yun Liu, Madhuran Jajoo, Chandrashekar Sankarapu, Swapnil Vispute, Harshad Purandare, Abhishek Bijay Mishra, Samuel Schmidgall, Tao Tu, Anil Palepu, Chunjong Park, Tim Strother, Rahul Thapa, Yong Cheng, Preeti Singh, Kat Black, Yossi Matias, Katherine Chou, Avinatan Hassidim, Kavi Goel, Joelle K. Barral, Tris Warkentin, Shravya Shetty, Dale R. Webster, Sunny Virmani, David F. Steiner, Can Kirmizibayrak, and Daniel Golden. MedGemma 1.5 technical report. *arXiv preprint arXiv:2604.05081*, 2026.
- [8] Zhanyu Wang, Lingqiao Liu, Lei Wang, and Luping Zhou. R2GenGPT: Radiology report generation with frozen LLMs. *arXiv preprint arXiv:2309.09812*, 2023.
- [9] Chunyuan Li, Cliff Wong, Sheng Zhang, Naoto Usuyama, Haotian Liu, Jianwei Yang, Tristan Naumann, Hoifung Poon, and Jianfeng Gao. LLaVA-Med: Training a large language-and-vision assistant for biomedicine in one day. In *NeurIPS*, 2023.
- [10] Michael Moor, Qian Huang, Shirley Wu, Michihiro Yasunaga, Yash Dalmia, Jure Leskovec, Cyril Zakka, Eduardo Pontes Reis, and Pranav Rajpurkar. Med-Flamingo: A multimodal medical few-shot learner. In *Machine Learning for Health Symposium, PMLR*, 2023.
- [11] Chunlei Li, Jingyang Hou, Yilei Shi, Jingliang Hu, Xiao Xiang Zhu, and Lichao Mou. Multimodal large language models for medical report generation via customized prompt tuning. *arXiv preprint arXiv:2506.15477*, 2025.
- [12] Tianwei Lin, Wenqiao Zhang, Sijing Li, Yuqian Yuan, Binhe Yu, Haoyuan Li, Wanggui He, Hao Jiang, Mengze Li, Xiaohui Song, et al. HealthGPT: A medical large vision-language model for unifying comprehension and generation via heterogeneous knowledge adaptation. In *ICML*, 2025.
- [13] Jing Jiao, Jin Zhou, Xiaokang Li, Menghua Xia, Yi Huang, Lihong Huang, Na Wang, Xiaofan Zhang, Shichong Zhou, Yuanyuan Wang, and Yi Guo. USFM: A universal ultrasound foundation model generalized to tasks and organs towards label-efficient image analysis. *Medical Image Analysis*, 96:103202, 2024.
- [14] Hongyuan Zhang, Yuheng Wu, Mingyang Zhao, Zhiwei Chen, Rebecca Li, Fei Zhu, Haohan Zhao, Xiaohua Yuan, Meng Yang, Chunli Qiu, Xiang Cong, Haiyan Chen, Lina Luan, Randolph H. L. Wong, Huai Liao, Colin A. Graham, Shi Chang, Guowei Tao, Dong Yi, Zhen Lei, Nassir Navab, Sébastien Ourselin, Jiebo Luo, Hongbin Liu, and Gaofeng Meng. A fully open and generalizable foundation model for ultrasound clinical applications. *arXiv preprint arXiv:2509.11752*, 2025.
- [15] Matthew Christensen, Miloš Vukadinovic, Neal Yuan, and David Ouyang. Vision-Language foundation model for echocardiogram interpretation. *Nature Medicine*, 30:1481–1488, 2024.

- [16] Miloš Vukadinovic, I-Min Chiu, Xiu Tang, Neal Yuan, Tien-Yu Chen, Paul Cheng, Debiao Li, Susan Cheng, Bryan He, and David Ouyang. Comprehensive echocardiogram evaluation with view-primed vision-language AI. *Nature*, 650:970–977, 2025.
- [17] Fadillah A. Maani, Numan Saeed, Tausifa Jan Saleem, Zaid Farooq, Hussain Alasmawi, Werner Diehl, Ameerah Mohammad, Gareth Waring, Saudabi Valappi, Leanne Bricker, and Mohammad Yaqub. FetalCLIP: A visual-language foundation model for fetal ultrasound image analysis. *npj Digital Medicine*, 2025.
- [18] Xiaoqing Guo, Mohammad Alsharid, He Zhao, Yipei Wang, Jayne Lander, Aris T. Papageorghiou, and J. Alison Noble. A visually grounded language model for fetal ultrasound understanding. *Nature Biomedical Engineering*, 2026.
- [19] Jiayun Jin, Haolong Chai, Xueying Huang, Xiaoqing Guo, Zengwei Zheng, Zhan Zhou, Junmei Wang, Xinyu Wang, Jie Liu, and Binbin Zhou. Ultrasound-CLIP: Semantic-Aware contrastive pre-training for ultrasound image-text understanding. In *CVPR*, 2026.
- [20] Taohan Weng, Chi Zhang, Chaoran Yan, Siya Liu, Xiaoyang Liu, Yalun Wu, Boyang Wang, Boyan Wang, Jiren Ren, Kaiwen Yan, Jinze Yu, Kaibing Hu, Henan Liu, Haoyun Zheng, Zhenyu Liu, Duo Zhang, Xiaoqing Guo, Anjie Le, and Hongcheng Guo. Dolphin v1.0 technical report. *arXiv preprint arXiv:2509.25748*, 2025.
- [21] Junhao Guo, Xuefeng Shan, Guoming Wang, Dong Chen, Rongxing Lu, and Siliang Tang. LLAUS: A high-quality instruction-tuned large vision language assistant for ultrasound. In *ICMR*, 2025.
- [22] Shijie Wang, Yilun Zhang, Zeyu Lai, and Dexing Kong. HAIBU-ReMUD: Reasoning multimodal ultrasound dataset and model bridging to general specific domains. *arXiv preprint arXiv:2506.07837*, 2025.
- [23] Dengbo Chen, Ziwei Zhao, Kexin Zhang, Shishuang Zhao, Junjie Hou, Yaqian Wang, Nianxi Liao, Anlan Sun, Fei Gao, Jia Ding, Yuhang Liu, and Dong Wang. UMind-VL: A generalist ultrasound vision-language model for unified grounded perception and comprehensive interpretation. *arXiv preprint arXiv:2511.22256*, 2025.
- [24] Chaoyin She, Ruifang Lu, Lida Chen, Wei Wang, and Qinghua Huang. EchoVLM: Dynamic mixture-of-experts vision-language model for universal ultrasound intelligence. *arXiv preprint arXiv:2509.14977*, 2025.
- [25] Haotian Liu, Chunyuan Li, Yuheng Li, and Yong Jae Lee. Improved baselines with visual instruction tuning. In *CVPR*, 2024.
- [26] Xiaokang Chen, Zhiyu Wu, Xingchao Liu, Zizheng Pan, Wen Liu, Zhenda Xie, Xingkai Yu, and Chong Ruan. Janus-Pro: Unified multimodal understanding and generation with data and model scaling. *arXiv preprint arXiv:2501.17811*, 2025.

Appendix

Case 1: Thyroid Examination (with suspected Hashimoto thyroiditis and multinodular goiter)



Human Report

Ultrasound Findings

Cervical lymph nodes: No abnormally enlarged lymph nodes are observed in the bilateral neck. Thyroid: The right thyroid lobe measures approximately 18 mm (AP) × 59 mm (SI) × 20 mm (transverse); the left lobe measures approximately 21 mm × 59 mm × 21 mm; the isthmus thickness is approximately 2 mm. The thyroid parenchyma demonstrates heterogeneous echogenicity. Multiple anechoic and mixed cystic-solid nodules are observed in both lobes. The largest lesion is located in the mid-to-lower portion of the right lobe, measuring approximately 15 × 11 × 13 mm, with relatively clear margins and regular morphology. Punctate vascular signals are observed within and around some nodules. No abnormal vascularity is observed within the thyroid gland.

Impression

Heterogeneous thyroid changes, suggestive of Hashimoto thyroiditis? Bilateral thyroid nodules, suggestive of nodular goiter?

LUMI

Ultrasound Findings

Cervical lymph nodes: No abnormally enlarged lymph nodes are observed in the bilateral neck. Thyroid: The right thyroid lobe measures approximately 22 mm (AP) × 56 mm (SI) × 25 mm (transverse); the left lobe measures approximately 20 mm × 56 mm × 23 mm; the isthmus thickness is approximately 5 mm. The thyroid parenchyma demonstrates decreased and heterogeneous echogenicity. Several isoechoic and mixed cystic-solid nodules are observed in both lobes. The largest lesion is located in the mid-to-lower portion of the right lobe, measuring approximately 20 × 11 × 15 mm, with relatively clear margins and regular morphology. Punctate and linear vascular signals are observed within and around some nodules. CDFI demonstrates no abnormal vascularity within the thyroid gland.

Impression

Heterogeneous thyroid enlargement, suggestive of Hashimoto thyroiditis?
Bilateral thyroid nodules, suggestive of nodular goiter? Other etiologies cannot be excluded.

Qwen3.5-27B

Ultrasound Findings

The thyroid parenchyma in both lobes demonstrates heterogeneous echogenicity with diffuse changes. A hypoechoic nodule is observed in the right thyroid lobe, with irregular morphology, indistinct margins, and heterogeneous internal echogenicity containing punctate hyperechoic foci. Hypoechoic areas are also observed in the left thyroid lobe. Color Doppler Flow Imaging (CDFI) demonstrates abundant vascularity within and around the right-lobe nodule, showing a 'fire-sea sign' appearance. Increased vascularity is also observed in the left lobe.

Impression

Diffuse thyroid disease, highly suggestive of thyroiditis (e.g., Hashimoto thyroiditis). Solid nodule in the right thyroid lobe (TI-RADS category 4); further evaluation, such as fine-needle aspiration biopsy, is recommended.

InternVL3.5-38B-Instruct

Ultrasound Findings

Multiple sections of the thyroid region are visualized in the provided ultrasound images. The bilateral thyroid lobes are normal in size and morphology with smooth capsules. The parenchymal echogenicity is homogeneous. A solid nodule is observed in the mid-pole of the right thyroid lobe, measuring approximately $1.2 \times 1.0 \times 0.8$ cm, with regular morphology, clear margins, and homogeneous hypoechoic internal echogenicity. CDFI demonstrates punctate vascular signals within the lesion, indicating internal vascularity.

Impression

Solid nodule in the right thyroid lobe (TI-RADS category 3); follow-up is recommended.

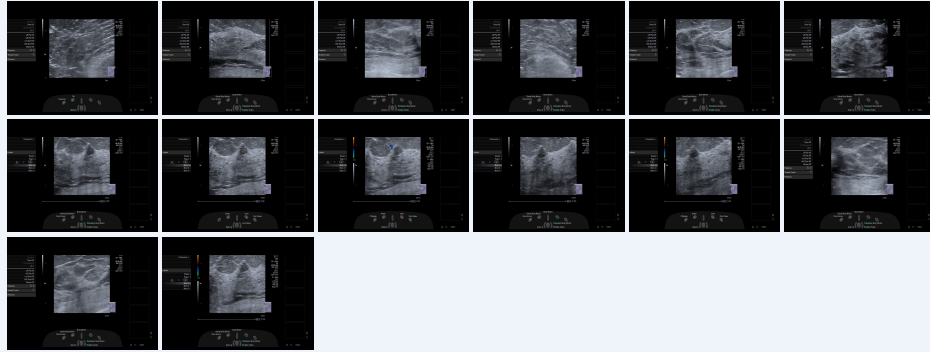
EchoVLM

Ultrasound Findings

Both thyroid lobes are normal in size, and the isthmus is not visualized. Two hypoechoic nodules are observed in the left lobe, with clear margins, aspect ratios less than 1, and scant vascularity. Two hypoechoic nodules are observed in the right lobe, with clear margins, aspect ratios less than 1, and scant vascularity. Multiple hypoechoic nodules are repeatedly described in both lobes with clear margins, aspect ratios less than 1, and scant vascularity.

Impression

Case 2: Breast Examination (with multiple right breast nodules)



Human Report

Ultrasound Findings

Bilateral breast structures are clearly visualized. The mammary ducts are not dilated. Multiple hypoechoic nodules are observed in the right breast, the largest located at the 10 o'clock position approximately 2 cm from the nipple, measuring approximately $0.5 \times 0.5 \times 0.6$ cm, with clear margins and relatively regular morphology. CDFI demonstrates no internal vascularity. No definite mass is observed in the left breast. No obvious abnormal lymph nodes are observed in the bilateral axillae.

Impression

Multiple hypoechoic nodules in the right breast, BI-RADS category 3; regular follow-up is recommended.

LUMI

Ultrasound Findings

The glandular architecture of both breasts is mildly disorganized. The mammary ducts are not dilated. A hypoechoic nodule is observed in the right breast at the 11 o'clock position approximately 3 cm from the nipple, measuring approximately $0.8 \times 0.8 \times 0.7$ cm, with indistinct margins and irregular morphology. Multiple punctate hyperechoic foci are observed within the lesion. CDFI demonstrates no internal vascularity. No definite mass is observed in the left breast. No obvious abnormal lymph nodes are observed in the bilateral axillae.

Impression

Hypoechoic nodule in the right breast, BI-RADS category 4A; contrast-enhanced ultrasound examination is recommended.

Qwen3.5-27B

Ultrasound Findings

On left breast scanning, a hypoechoic mass is observed in the left breast with irregular lobulated morphology, indistinct margins, and angular projections in some areas. The lesion demonstrates heterogeneous internal echogenicity with mixed hypoechoic components. The lesion is taller-than-wide. No obvious posterior acoustic enhancement or attenuation is observed. CDFI demonstrates punctate vascular signals within and around the lesion.

Impression

Solid lesion in the left breast with irregular morphology, BI-RADS category 4; further evaluation such as biopsy is recommended.

InternVL3.5-38B-Instruct

Ultrasound Findings

The breast parenchyma demonstrates homogeneous echogenicity without obvious abnormal structures. A hypoechoic lesion is observed in the mid portion of the right breast, measuring approximately 1.2 × 0.8 × 0.6 cm, with regular morphology, clear margins, and homogeneous internal hypoechoogenicity. CDFI demonstrates no obvious internal vascularity.

Impression

Hypoechoic lesion in the right breast (BI-RADS category 3); follow-up is recommended.

EchoVLM

Ultrasound Findings

Ultrasound Findings: No obvious abnormal lesions are observed in either breast. No dilatation of the mammary ducts is observed. No obvious space-occupying lesions are identified. No abnormal vascularity is observed in either breast. No abnormal lymph nodes are observed in the bilateral axillae. Ultrasound

Impression: No obvious abnormal lesions in either breast.

Impression

Case 3: Upper Abdomen Examination (with fatty liver, multiple benign hepatic lesions, hepatic cysts, and gallbladder polyps)



Human Report

Ultrasound Findings

The liver is enlarged with a smooth surface and blunt edges. Multiple hypoechoic lesions are observed within the liver. The largest lesion is located in the superior segment of the right posterior lobe, measuring approximately $3.2 \times 3.1 \times 4.1$ cm, with indistinct margins but relatively regular morphology. CDFI demonstrates no internal vascularity. Multiple cystic lesions are additionally observed within the liver, the largest located in the superior segment of the left lateral lobe, measuring approximately $2.8 \times 2.2 \times 2.3$ cm, with clear margins. The remaining liver parenchyma demonstrates slightly increased fine echogenicity with mild posterior attenuation. Intrahepatic vessels are relatively well visualized. The main portal vein is within normal limits. No dilatation of the intrahepatic or extrahepatic bile ducts is observed. The gallbladder is normal in size and morphology with a mildly irregular wall. Multiple hyperechoic nodules are observed along the gallbladder wall, the largest measuring approximately $0.6 \times 0.5 \times 0.5$ cm, without acoustic shadowing or positional mobility. The pancreas and spleen are normal in size and morphology with homogeneous echogenicity. No definite focal lesions are identified, and neither the pancreatic duct nor splenic vein is significantly dilated.

Impression

1. Fatty liver. 2. Multiple hypoechoic hepatic lesions, likely benign, without significant interval change compared with prior examination. 3. Multiple hepatic cysts. 4. Multiple polypoid lesions of the gallbladder wall.

LUMI

Ultrasound Findings

The liver is enlarged with a smooth surface and blunt edges. Multiple cystic lesions are observed within the liver. The largest lesion is located in the right hepatic lobe, measuring approximately 2.8 × 2.2 × 2.3 cm, with clear margins and regular morphology. CDFI demonstrates no internal vascularity. A heterogeneous hypoechoic lesion is observed in the right hepatic lobe, measuring approximately 3.2 × 3.2 × 4.1 cm, with relatively clear margins and relatively regular morphology. CDFI demonstrates no internal vascularity. The remaining liver parenchyma demonstrates slightly increased fine echogenicity with mild posterior attenuation. Intrahepatic vessels are not clearly visualized. The main portal vein is within normal limits. No dilatation of the intrahepatic or extrahepatic bile ducts is observed. The gallbladder is normal in size and morphology with a mildly irregular wall. Multiple mildly hyperechoic nodules are observed along the gallbladder wall, the largest measuring approximately 0.6 × 0.5 cm, without acoustic shadowing or positional mobility. No obvious abnormality is observed in the pancreas or spleen.

Impression

1. Heterogeneous hypoechoic lesion in the right hepatic lobe; contrast-enhanced ultrasound examination is recommended. 2. Multiple hepatic cysts. 3. Fatty liver. 4. Multiple polypoid lesions of the gallbladder wall.

Qwen3.5-27B

Ultrasound Findings

The liver is normal in size and morphology with a smooth capsule. The hepatic parenchyma demonstrates coarse echogenicity with relatively homogeneous distribution. A mildly hyperechoic lesion is observed in the right hepatic lobe, with clear margins and regular morphology, measuring approximately 3.2 × 3.2 cm. Multiple anechoic lesions are observed within the liver, the largest located in the right lobe, round in shape with clear margins and posterior acoustic enhancement, measuring approximately 2.8 × 2.2 cm. Another smaller cystic lesion measures approximately 1.5 × 1.4 cm. The gallbladder is normal in size and morphology without wall thickening or definite intraluminal abnormal echogenicity. A hyperechoic focus measuring approximately 0.5 cm is observed near the gallbladder neck/cystic duct region. The main portal vein diameter is normal. CDFI demonstrates good portal venous flow filling with hepatopetal flow. No significant abnormalities are identified in the pancreas, spleen, or bilateral kidneys.

Impression

1. Solid lesion in the right hepatic lobe, most likely hepatic hemangioma; regular follow-up is recommended. 2. Multiple hepatic cysts. 3. Gallbladder stone in the neck/cystic duct region. 4. Coarse hepatic echogenicity, suggestive of fatty liver or chronic liver injury.

InternVL3.5-38B-Instruct

Ultrasound Findings

Multiple sections of the liver at different locations are visualized in the provided ultrasound images. The hepatic parenchyma demonstrates homogeneous echogenicity without obvious abnormal focal lesions. Multiple hypoechoic lesions of varying sizes with clear margins are observed in some images. CDFI demonstrates no internal vascularity within these lesions. In addition, the liver is normal in size and morphology without obvious enlargement or atrophy.

Impression

Multiple hypoechoic hepatic lesions, likely hepatic cysts or hemangiomas; follow-up is recommended.

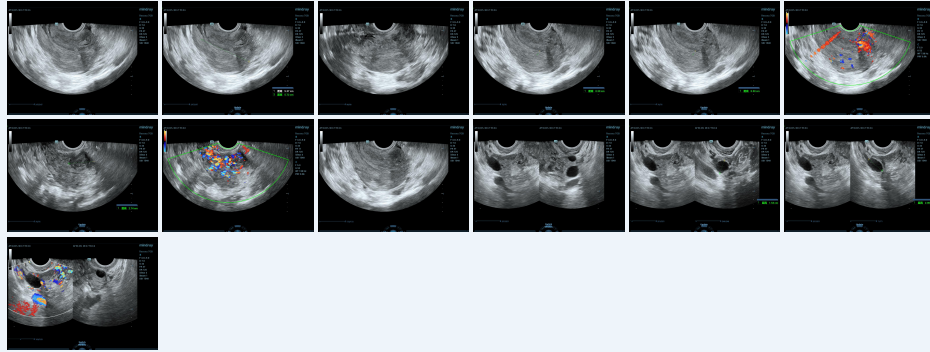
EchoVLM

Ultrasound Findings

The liver is normal in size and morphology with a smooth surface and homogeneous parenchymal echogenicity. The hepatic vein diameter is normal. No dilatation of the intrahepatic bile ducts is observed. The phrase 'no dilatation of the intrahepatic bile ducts' is repeatedly generated throughout the report.

Impression

Case 4: Gynecology Examination (with uterine fibroids and a suspected mesosalpinx cyst)



Human Report

Ultrasound Findings

The uterus is retroverted, measuring approximately $5.4 \times 5.7 \times 4.8$ cm. The endometrium is centrally located with a single-layer thickness of approximately 0.25 cm. Two to three hypoechoic lesions are observed within the myometrium, the largest located in the right posterior intramural wall with slight subserosal protrusion, measuring approximately 2.7 cm in diameter, with clear margins and peripheral vascularity detected on Doppler imaging. A cystic lesion measuring approximately 2.0 cm in diameter is observed adjacent to the right ovary, with a thin wall and clear cystic fluid. No obvious vascularity is observed within the cyst wall. No definite mass is identified in the left adnexal region.

Impression

Uterine fibroids. Right paraovarian cystic lesion, suspicious for mesosalpinx cyst.

LUMI

Ultrasound Findings

The uterus is retroverted, measuring approximately $5.4 \times 5.7 \times 5.1$ cm. The endometrium is centrally located with a single-layer thickness of approximately 0.25 cm. A hypoechoic lesion measuring approximately 2.7 cm in diameter is observed in the right fundal intramural myometrium, with clear margins and peripheral vascularity detected on Doppler imaging. A cystic lesion measuring approximately 2.0 cm in diameter is observed adjacent to the right ovary, with clear cystic fluid and vascularity detected in the cyst wall. A cystic lesion measuring approximately 1.5 cm in diameter is observed adjacent to the left ovary, with clear cystic fluid and vascularity detected in the cyst wall.

Impression

Uterine fibroid. Bilateral paraovarian cystic lesions.

Qwen3.5-27B

Ultrasound Findings

Transvaginal ultrasound examination demonstrates an anteverted uterus with enlarged size and full morphology. The myometrium demonstrates heterogeneous echogenicity with multiple hypoechoic and mildly hyperechoic mass-like lesions with relatively clear margins. A larger round hypoechoic lesion is observed in the lower anterior uterine wall, measuring approximately 5.72 × 5.37 cm, with heterogeneous internal echogenicity and no obvious posterior attenuation. A smaller hypoechoic lesion measuring approximately 2.74 cm is observed in the posterior uterine wall. CDFI demonstrates relatively abundant vascularity within and around these lesions. The endometrial stripe is displaced posteriorly but remains clearly visualized, with thickness approximately 0.50 cm. Bilateral adnexal cystic lesions are observed. A larger anechoic lesion is observed in the right adnexal region, measuring approximately 2.00 × 1.54 cm, with regular morphology, clear margins, and posterior acoustic enhancement. Similar cystic lesions are observed in the left adnexal region. CDFI demonstrates no obvious abnormal vascularity within the cyst walls or surrounding regions. No obvious pelvic free fluid is observed.

Impression

1. Multiple uterine fibroids with relatively abundant vascularity. 2. Bilateral ovarian cysts, the largest measuring approximately 2.0 × 1.5 cm in the right adnexal region. 3. Clinical follow-up is recommended.

InternVL3.5-38B-Instruct

Ultrasound Findings

The uterus is normal in size and morphology without obvious abnormal intracavitary echogenicity. A mixed-echogenic lesion measuring approximately 5.7 × 5.7 cm is observed in the posterior uterine wall, with relatively clear margins and heterogeneous internal echogenicity. CDFI demonstrates abundant internal vascularity. No obvious abnormalities are identified in the bilateral adnexal regions.

Impression

Mixed-echogenic lesion in the posterior uterine wall, likely uterine fibroid; further evaluation and follow-up are recommended.

EchoVLM

Ultrasound Findings

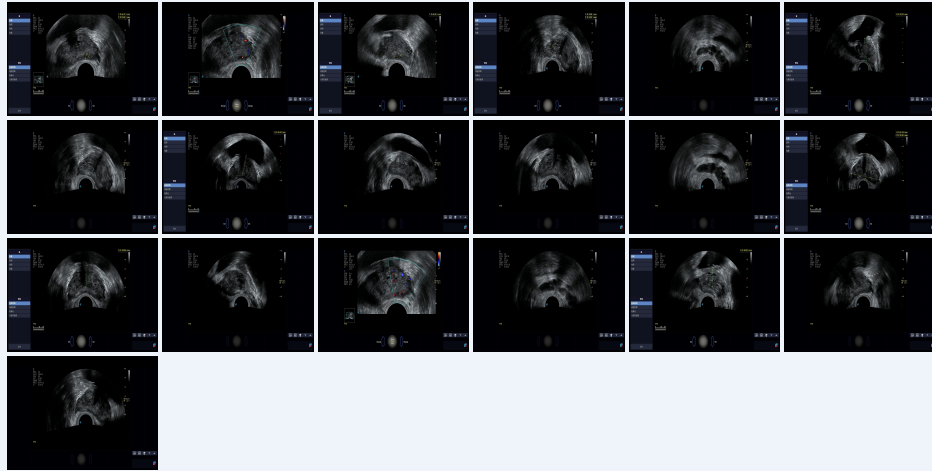
The uterus is normal in size and morphology. Multiple anechoic lesions are observed within the uterine cavity, the largest located in the mid cavity measuring 33 × 25 × 24 mm, with clear margins, smooth walls, and no obvious vascularity. The myometrium demonstrates homogeneous echogenicity without obvious abnormality. Bilateral ovaries are normal in size and morphology without

obvious abnormality. No abnormality is observed in the bilateral adnexal regions. CDFI demonstrates no obvious abnormal vascularity.

Impression

The uterus is normal in size and morphology. A gestational sac measuring approximately 5.4 × 5.7 cm is observed within the uterine cavity, containing an embryo measuring approximately 0.5 cm without detectable fetal cardiac activity. The myometrium demonstrates homogeneous echogenicity without obvious abnormality. Bilateral ovaries are normal in size and morphology without obvious abnormality. No abnormalities are observed in the bilateral adnexal regions. The endometrium demonstrates homogeneous echogenicity with a thickness of approximately 1.5 cm. A hypoechoic lesion measuring approximately 2.7 × 2.0 cm is observed beneath the endometrium, with irregular morphology, indistinct margins, heterogeneous internal echogenicity, and no obvious vascularity.

Case 5: Male Urinary Examination (with benign prostatic hyperplasia, prostatic cysts, and a suspicious prostatic lesion)



Human Report

Ultrasound Findings

Transrectal ultrasound examination was performed. The prostate measures 5.6 cm in transverse diameter, 3.5 cm in anteroposterior diameter, 2.6 cm in anteroposterior diameter of the transitional zone, and 3.4 cm in craniocaudal diameter. The estimated prostate weight is 35 g (reference values: mild hyperplasia 20–25 g, moderate hyperplasia 26–50 g, severe hyperplasia >50 g). The prostate demonstrates enlarged volume with preserved contour, intact capsule, and symmetrical morphology. The transitional zone and peripheral zone are clearly demarcated. The transitional zone demonstrates heterogeneous nodular echogenicity. Multiple punctate hyperechoic foci are observed within the parenchyma, consistent with calcifications. Multiple cysts are additionally observed, the largest measuring approximately 0.4 × 0.3 cm. A hypoechoic lesion is observed in the left peripheral zone, measuring approximately 0.7 × 0.4 × 0.7 cm, with indistinct margins. CDFI demonstrates no internal vascularity. Bilateral seminal vesicles are clearly visualized without obvious abnormality.

Impression

1. Benign prostatic hyperplasia with prostatic calcifications. 2. Multiple prostatic cysts. 3. Hypoechoic lesion in the left peripheral zone of the prostate; MRI examination is recommended, and ultrasound-guided biopsy may be considered if necessary.

LUMI

Ultrasound Findings

Transrectal ultrasound examination was performed. The prostate measures approximately 5.5 cm in transverse diameter, 3.5 cm in anteroposterior diameter, 2.9 cm in anteroposterior diameter of the transitional zone, and 3.3 cm in craniocaudal diameter. The estimated prostate weight is 33 g (reference values: mild hyperplasia 20–25 g, moderate hyperplasia 26–50 g, severe hyperplasia >50 g). The prostate demonstrates enlarged volume with preserved contour, intact capsule, and symmetrical morphology. The transitional zone and peripheral zone are clearly demarcated. The transitional zone demonstrates heterogeneous nodular echogenicity. Multiple patchy hyperechoic foci are observed within the parenchyma, consistent with calcifications. Multiple cysts are additionally observed, the largest measuring approximately 0.4 × 0.3 cm. A hypoechoic lesion is observed in the right peripheral zone, measuring approximately 0.7 × 0.4 × 0.7 cm, with clear margins and regular morphology. CDFI demonstrates no internal vascularity. Bilateral seminal vesicles are clearly visualized without obvious abnormality.

Impression

1. Hypoechoic lesion in the right peripheral zone of the prostate; correlation with serum PSA and MRI examination is recommended. 2. Benign prostatic hyperplasia with prostatic calcifications. 3. Multiple prostatic cysts.

Qwen3.5-27B

Ultrasound Findings

Transvaginal ultrasound examination demonstrates an anteverted uterus with enlarged size and full morphology. The myometrium demonstrates heterogeneous echogenicity with multiple hypoechoic nodules and mass-like lesions with relatively clear margins. A larger hypoechoic lesion is observed in the posterior uterine wall, measuring approximately 5.6 × 3.5 cm, with relatively homogeneous internal echogenicity and several small cystic areas. Additional smaller hypoechoic nodules are observed in the anterior and lateral uterine walls, some measuring approximately 3.4 × 2.8 cm. CDFI demonstrates punctate and linear vascular signals within and around these lesions. The endometrial stripe is clearly visualized without obvious abnormality.

Impression

1. Multiple uterine fibroids. 2. Enlarged uterus.

InternVL3.5-38B-Instruct

Ultrasound Findings

The uterus is normal in size and morphology with homogeneous endometrial thickness. A hypoechoic lesion is observed in the posterior uterine wall, measuring approximately 12.43 × 10.28 × 9.14 mm, with clear margins and heterogeneous internal echogenicity. CDFI demonstrates minimal internal vascularity.

Impression

Posterior uterine wall fibroid (FI-RADS category 3); follow-up is recommended.

EchoVLM

Ultrasound Findings

The uterus is normal in size and morphology. Multiple anechoic lesions are observed within the uterine cavity, the largest located in the mid cavity measuring 33 × 25 × 24 mm, with clear margins, smooth walls, and no obvious vascularity. The myometrium demonstrates homogeneous echogenicity without obvious abnormality. Bilateral ovaries are normal in size and morphology without obvious abnormality. No abnormality is observed in the bilateral adnexal regions. CDFI demonstrates no obvious abnormal vascularity.

Impression

Multiple anechoic lesions within the uterine cavity, suggestive of intrauterine fluid collection or intracavitary lesions. Further evaluation, such as hysteroscopy or intracavitary ultrasound examination, is recommended.